Research Article

An improved method for high photocatalytic performance of ZnAl$_2$O$_4$ spinel derived from layered double hydroxide precursor

Ageng Trisna Surya Pradana Putra[1] ⓘ

Abstract

A spinel structure of zinc aluminate (ZnAl$_2$O$_4$) particles provides a prospective material for photocatalytic applications. In this work, zinc aluminate spinel was prepared by an anion-exchange method derived from layered double hydroxides (LDHs) followed by thermal treatment. The mechanism, photoactivity, and effects of both anion substitute and temperature have been investigated. The chemical composition, morphologies, phase structures, porous structures and photocatalytic properties of samples were analyzed using thermogravimetric analysis, scanning electron microscopy, energy-dispersive X-ray spectroscopy, powder X-ray diffraction, gas sorption analysis, and ultraviolet–visible spectroscopy in detail. The results of mesoporous α-ZnAl$_2$O$_4$ indicate that average crystallite size, total pore volume, and BET surface area obtain 9.3 nm, 0.337 cm^3/g, and 206.13 m^2/g, respectively. Moreover, zinc aluminate spinel shows well phase after heating at 700 °C and LDHs structures were completely collapsed. The photocatalytic performances of α-ZnAl$_2$O$_4$ have been applied in p-nitrophenol reduction under visible light irradiation and required time at least 9 min. Finally, the new improved method constructs an excellent material for pretreatment of liquid pollutants containing high-level concentration at rapid treatment time.

Keywords Layered double hydroxide · Water treatment · Liquid pollutants · Photocatalysis · Zinc aluminate spinel

1 Introduction

Liquid pollutants discharged from cosmetic, paper printing, textile, and other industries contaminate the ecosystem and cause serious implications for animals, plants, and other organisms in aquatic life. Among phenolic compounds, p-nitrophenol (hereafter pNP) is widely applied in various industries, but pNP as a recalcitrant organic contaminant obtains high toxicity in the aquatic environment [1–3]. Recently, several techniques such as adsorption [4], advanced oxidation [5], biological treatment [6], coagulation and flocculation [7] have been developed to reduce phenolic compounds from watery solutions. Nevertheless, the materials for the removal of pNP obtain complicated problems, including low surface area and pore volume.

Therefore, finding an inexpensive cost, the environmentally friendly method is necessary for handling industrial wastewater containing phenolic compounds.

Semiconductor photocatalysis is a prospective method to remove credential organic pollutants in wastewater. Up to now, numerous active-photocatalysts such as CuO [8], Fe$_2$O$_3$ [9], SnO$_2$ [10], TiO$_2$ [11], WO$_3$ [12], and ZnO [13] are highly potential applications in various industries. For an effective candidate and an efficient treatment, the development of photocatalysts with high pore volume and surface area is essential. Furthermore, the previous semiconductors obtain fundamental problems such as high cost and low rates of degradation. Therefore, an excellent technique is being applied to the expandable properties of photocatalysts. This solution can be modified by

✉ Ageng Trisna Surya Pradana Putra, ageng.trisna@uinbanten.ac.id | [1]Faculty of Science and Technology, Universitas Islam Negeri Sultan Maulana Hasanuddin, Serang 42118, Indonesia.

compositions and morphologies of the materials. Recently, several mixed metal oxides with spinel structures as photocatalysis applications under solar light irradiation have been discussed for the treatment of organic contaminants in water [14–17].

Mixed metal oxides, also known as spinels, have been broadly reported for their great applications in the subjects of catalysis [18, 19], adsorption [20, 21], electrochemistry [22], and others. Spinels contain cationic and anionic sites with a 3:4 ratio, respectively. These materials can be represented by the general formula AB_2X_4, A and B refer to cations and X describes anion. Based on their anions, the spinels possess three groups such as oxyspinel (O^{2-}), selenospinel (Se^{2-}), and thiospinel (S^{2-}). These groups obtain several subgroups such as spinel ($A^{2+} B^{3+}_2 O_4$), ulvöspinel ($A^{4+} B^{2+}_2 O_4$), bornhardtite ($A^{2+} B^{3+}_2 Se_4$), tyrrellite ($A^{1+} B^{3:5+}_2 Se_4$), carrollite ($A^{1+} B^{3:5+}_2 S_4$), and linnaeite ($A^{2+} B^{3+}_2 S_4$) [23]. Most especially, spinels offer an efficient path [24], high catalytic activity [25], improved stability [26], useful catalyst [27–30], and great recyclability [31]. The chemical structure of binary spinel (AB_2O_4) can be replaced by divalent ($A = Zn^{2+}$) and trivalent ($B = Fe^{3+}$) metal ions, resulting in photocatalytically active microstructure of zinc ferrite ($ZnFe_2O_4$) [32]. Furthermore, the atomic ratio between A^{2+} and A^{3+}/A^{4+} acquired high catalytic activity for dye degradation [33, 34]. Nowadays, the solar-responsive spinel photocatalyst has been presented as a potential material for application in wastewater treatments [35]. Besides, oxyspinels have been studied as excellent photocatalytic degradation for methylene blue [36, 37] and methyl orange [38].

Meanwhile, several oxyspinels were prepared from inorganic anions (carbonate, nitrate, phosphate, and sulfate) pillared A^{2+}–A^{3+} layered double hydroxides and followed by a thermal process that they performed the improved catalytic activities [39–46]. Afterward, we study the improved photocatalytic degradation of pNP through a solar-responsive oxyspinel derived from organic anion pillared LDH precursors under UV-light irradiation.

The aims of this work were to investigate the effects of both anion replacement and thermal treatment of starting organic anion pillared LDH precursors and to study mechanism and photoactivity of the catalyst candidate for removing an organic pollutant in wastewater.

2 Experimental section

2.1 Materials

In this experiment, aluminum nitrate nonahydrate ($Al(NO_3)_3\cdot9H_2O$), p-nitrophenol (pNP, > 99%), and sodium borohydride ($NaBH_4$) were acquired from Aladdin Chemical Co. Ltd. Sodium hydroxide (NaOH), kalium hydroxide

(KOH), and N,N-dimethylformamide (DMF, 99.5%) were provided by Xilong Chemical. Zinc nitrate ($Zn(NO_3)_2\cdot6H_2O$, 98%) and perylene 3,4,9,10-tetracarboxylic dianhydride (PTCDA, 97%) were used as supplied by Sigma-Aldrich. All chemicals were analytical grade and without further purification before use.

2.2 Synthesis of NO_3^- (H_2O) ZnAl-layered double hydroxide (LDH)

The ZnAl-NO_3-LDH (hereafter ZAN-LDH) was prepared using a co-precipitation technique. Firstly, the solution containing 0.1 M $Zn(NO_3)_2\cdot6H_2O$ and 0.05 M $Al(NO_3)_3\cdot9H_2O$ was dissolved in CO_2-free deionized water to form a blended solution. Secondly, the mixed solution was added by NaOH (2 M) until pH 7 in nitrogen ambience to avoid impurity by carbon dioxide. The third point, the resulted slurry was aged at 70 °C for 18 h. Also, the suspension was centrifuged and washed with sterile water repeatedly. Finally, the solid material was dried in the oven at 80 °C overnight.

2.3 Synthesis of perylene-3,4,9,10-tetracarboxylic acid

Perylene-3,4,9,10-tetracarboxylic acid (abbreviated as PTCA) was synthesized from hydrolyzed perylene-3,4,9,10-tetracarboxylic dianhydride (hereafter PTCDA) according to previous reported literatures [47, 48]. The PTCDA (1 mmol) was dissolved by 5% KOH solution under stirring between 60 and 70 °C. Furthermore, the solution was adjusted to acid (pH 5–6) with 0.1 M HCl after cooling to ambient temperature. In addition, the red suspension was filtered from the solution and the solid yield was directly dried in vacuum.

2.4 Synthesis of PTCA (DMF) ZnAl LDH

PTCA-intercalated LDH (denoted as ZAP-LDH) was prepared by an ion-exchange method as following: 1 gr ZAN-LDH product was dispersed in 50 mL distilled water and added to 0.5 g PTCA dissolved in 50 mL DMF. Furthermore, the suspension was adjusted at neutral condition (pH 7) using 2 M NaOH and vigorously stirred for 6 h at 70 °C. Besides, the obtained product was recovered by filtration, washed with deionized water, and dried at 80 °C overnight.

2.5 Synthesis of $ZnAl_2O_4$ spinel derived from ZAP-LDH

The calcination of solid material was constructed by heating at 700 °C and 800 °C. The dried precipitates were loaded to a ceramic boat holder, heated into a tubular

furnace to the required temperatures and the heating rate was maintained at 5 °C min^{-1} combined with argon inflow. Each product was labeled as α-ZnAl$_2$O$_4$ and β-ZnAl$_2$O$_4$, where ZnAl$_2$O$_4$ describes calcined ZAP-LDH. Also, α and β represent the temperature of the thermal process at 700 °C and 800 °C, respectively.

2.6 Structural characterizations

All samples were characterized by PXRD, SEM, EDX, TGA-DTA, N$_2$ adsorption–desorption, and UV–Vis spectroscopy. The PXRD patterns for ZAN-LDH, PTCA, ZAP-LDH, α-ZnAl$_2$O$_4$, and β-ZnAl$_2$O$_4$ were performed using a SHIMADZU LabX XRD-6000 with Cu radiation at 40 kV and 30 mA (2θ in the range 3–70° for ZAN-LDH, PTCA, ZAP-LDH, and the range from 20° to 70° for α-ZnAl$_2$O$_4$ and β-ZnAl$_2$O$_4$). The average crystal size in nm (D_{XRD}) was calculated from XRD peaks using Scherrer's formula (1):

$$D_{XRD} = \frac{(0.9 \cdot \lambda)}{(\beta \cdot cos\theta)} \tag{1}$$

where β, λ, and θ represent the full width at half maximum or FWHM of peak (radian), the wavelength of Cu Kα radiation (1.54056 Å), and the Bragg angle (°), respectively.

The surface morphology of solid products and UV–Vis absorbance spectra of the catalyst samples in the region of 250–475 nm were observed by a JSM-6510A field-emission scanning electron microscope and a SHIMADZU UV-2450, respectively. The EDX spectra of chemical composition were obtained using JEOL JED-2300 at the accelerating voltage of 20 kV. In addition, thermogravimetric analyses at a heating rate of 10 °C min^{-1} in nitrogen atmosphere from environmental temperature to 700 °C were recorded on a SHIMADZU DTG-60 and N$_2$ adsorption–desorption measurements at liquid nitrogen temperature (− 196 °C) were determined using a Micromeritics instruments TriStar II 3020.

2.7 UV-light photocatalytic performance

Photocatalytic degradation of pNP was prepared by taking 0.025 mL pNP (0.6 mM and pH ~ 12), 0.75 mL NaBH$_4$ (0.2 M), and 2.7 mL distilled water in test tubes containing 20 mg of catalyst. All tests were repeated in duplicate and a blank evaluation was also analyzed by the same procedure without a catalyst. The decolorization of pNP due to adsorption was measured from initial and final observations.

3 Results and discussion

3.1 X-ray powder diffraction analysis

Investigated materials, such as average crystallite size and phase structure from diffractograms, are shown in Fig. 1. The ZAN-LDH was synthesized by the co-precipitation technique in H$_2$O at 70 °C. Typical properties of ZAN-LDH as a precursor were confirmed by a PXRD measurement. Furthermore, the representative signals are observed peaks at 2θ = 9.951°, 19.891°, and 29.494° corresponding to the (003), (006), and (009) planes, respectively. Consequently, the angle of nitrate ion can be determined less than 90° from the host layers.

The ZAP-LDH was prepared by an anion-exchange route from the ZAN-LDH precursor in DMF at 70 °C. New X-ray diffraction peaks of ZAP-LDH obtain at 2θ = 4.853°, 9.865°, and 14.258°, which can be indexed to (003), (006), and (009) planes, respectively. Therefore, a new basal spacing (d_{003} = 1.82 nm) represents evidence of new pillared material. The nitrate in the interlayer structure of ZAN-LDH is replaced by the PTCA-organic compound indicating relatively weak interaction between layered sheets and NO$_3^-$ anion. The illustration of PTCA intercalated LDH interlayers is presented in Scheme 1.

The ZAP-LDH has electrostatically interacted between layered sheets and carboxylate groups of PTCA as an intercalated complex. The interaction of negatively charged PTCA, positively charged layers, and water confirms hydrogen-bonding. Furthermore, the XRD pattern of ZAP-LDH presents two significant parameters such as a and c. The a parameter defines average cation-cation length within layers (2d_{110}) and also c parameter describes Coulomb
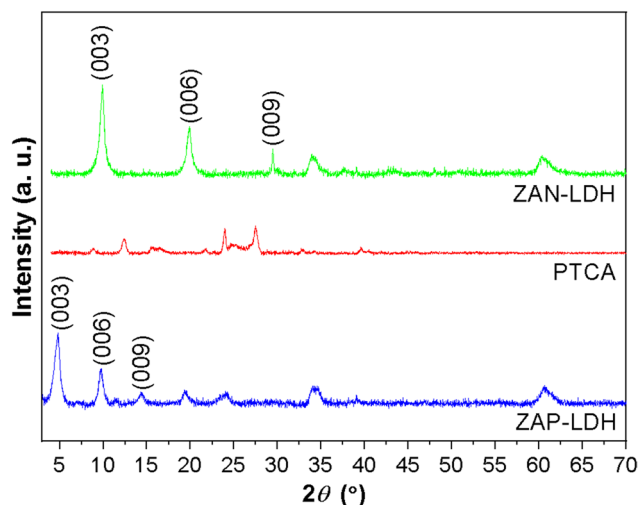

Fig. 1 PXRD diffractograms of ZAN-LDH, PTCA, and ZAP-LDH

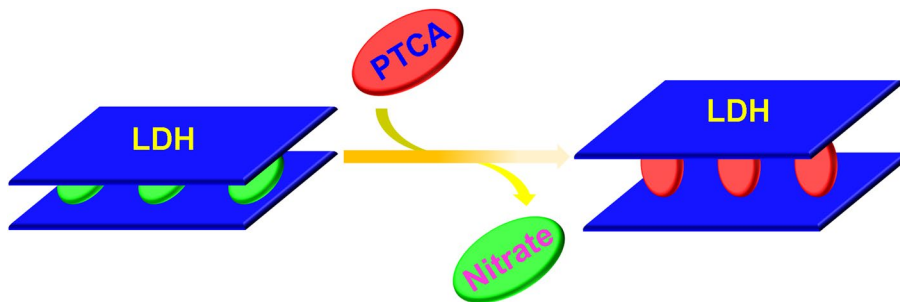**Scheme 1** Schematic representation of PTCA intercalated LDH interlayers

Table 1 Indexing of XRD patterns for ZAN-LDH and ZAP-LDH

Parameter	ZAN-LDH	ZAP-LDH
d_{003} (nm)	0.89	1.82
d_{006} (nm)	0.44	0.90
d_{009} (nm)	0.30	0.62
d_{110} (nm)	0.15	0.15
lattice parameter a (nm)	0.30	0.30
lattice parameter c (nm)	2.67	5.46
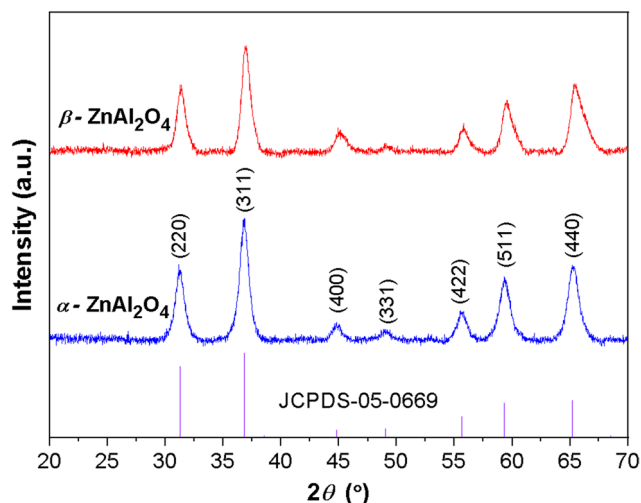
Fig. 2 X-ray diffraction patterns of α-ZnAl$_2$O$_4$ and β-ZnAl$_2$O$_4$

force between layer and anion in interlayer spacing ($3d_{003}$). Accordingly, the c-axis value of ZAP-LDH material shows an increase. Table 1 presents the indexing of X-ray patterns between ZAN-LDH and ZAP-LDH.

Thermal evolution constructs ZAP-LDH into ZnAl$_2$O$_4$, a spinel structure. Besides, the specific surface area of ZnAl$_2$O$_4$ increases in size after calcination treatment. Furthermore, the calcined product obtains centered cubic spinel phases (JCPDS No. 05-0669) as ZnAl$_2$O$_4$ and diffraction peaks at 2θ = 31.4°, 36.9°, 44.8°, 49.1°, 55.7°, 59.4°, and 65.3°, corresponding to the reflections from (220), (311), (400), (331), (442), (511), and (440) crystal planes, respectively.

Figure 2 shows the X-ray patterns of the spinel obtained at calcination temperatures at 700 °C (α-ZnAl$_2$O$_4$) and 800 °C (β-ZnAl$_2$O$_4$).

The standard crystal of the ZnAl$_2$O$_4$ spinel obtained a good index at different temperatures in which the material equals a cubic configuration and acquires a good crystallinity. Based on Scherrer's equation, the average sizes of α-ZnAl$_2$O$_4$ and β-ZnAl$_2$O$_4$ specimens calculated on the peak at 2θ = 36.75° are 9.3 nm and 10.1 nm, respectively.

3.2 Thermogravimetric analysis and differential thermal analysis

Figure 3 illustrates the TGA-DTA curves between ZAN-LDH and ZAP-LDH under nitrogen gas. Two endothermic points at 90 °C and 230 °C prove removal from interlayer water (3.9%) and dehydroxylation (12.2%), respectively (Fig. 3a). In contrast, the endothermic peaks indicate displacement of weakly adsorbed water at 69 °C and removal of interlayer water at 181 °C. Further, nitrate ions decomposition yields 22% at a temperature between 304 °C and 582 °C. Moreover, a strong exothermic peak denotes the decomposition of PTCA (34%) at 482 °C (Fig. 3b).

3.3 Brunauer–Emmett–Teller surface area analysis

The nitrogen adsorption-desorption isotherms illustrate in Fig. 4. On the one hand, the ZAP-LDH obtains a microporous structure and follows type I sorption isotherm, indicating relatively small external surfaces and successfully intercalated by PTCA as a pillared compound. The ZAP-LDH results a significant porosity and an important surface area at least 72.96 m^2/g. The type I corresponds with activated carbons, molecular sieve zeolites, and porous oxides.

On the other hand, type IV isotherms with H3 hysteresis loops are followed by α-ZnAl$_2$O$_4$ and β-ZnAl$_2$O$_4$, indicating a mesoporous scale. Calcined samples apply to rise slit-shaped pores and to improve specific surface area. The increasing temperature between 700 and 800 °C significantly reduces the specific surface area from 206.13 to 155.79 m^2/g. In addition, the heating process shapes crystalline ZnAl$_2$O$_4$, but the carbonization removes organics

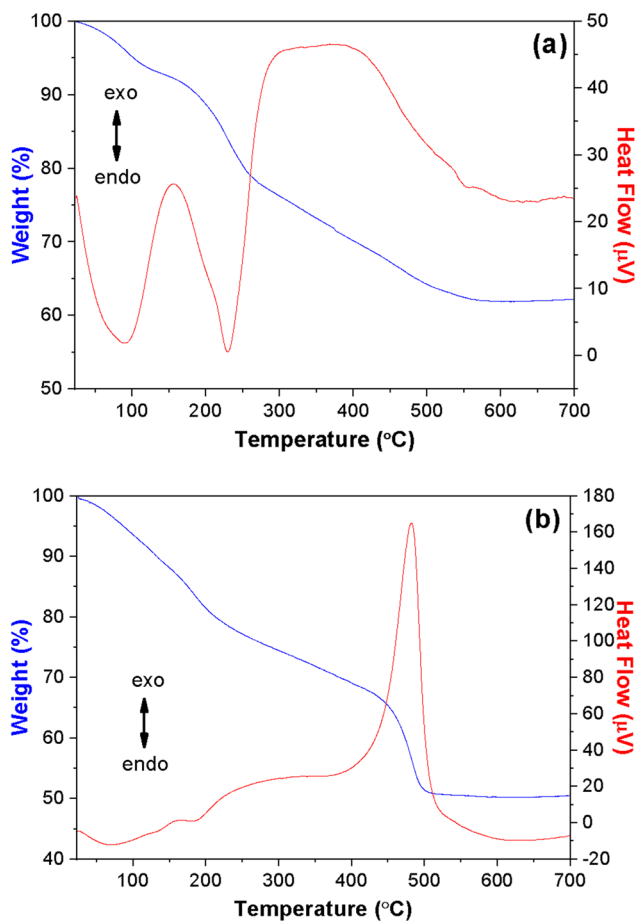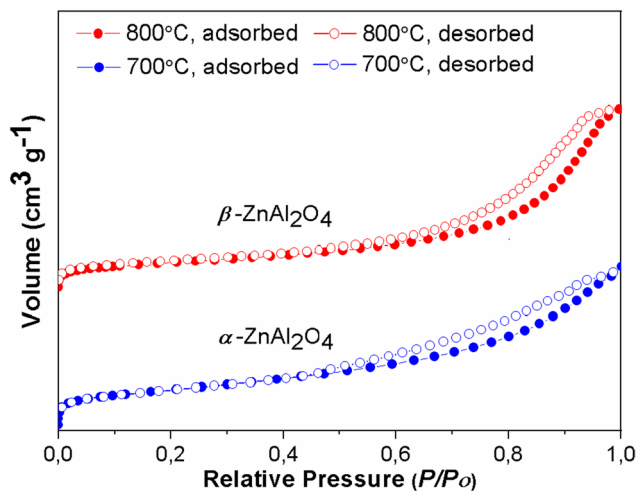**Fig. 3** TGA-DTA curves of ZAN-LDH (**a**) and ZAP-LDH (**b**)

Fig. 4 Nitrogen (N_2) adsorption–desorption isotherm curve of α-ZnAl$_2$O$_4$ and β-ZnAl$_2$O$_4$

as carbon cores and water from material to obtain porous particles. The surface area, pore volume, and average size of the samples are summarized in Table 2.

Table 2 Specific surface area values of ZAP-LDH, α-ZnAl$_2$O$_4$, and β-ZnAl$_2$O$_4$

Sample	S_{BET}[a]	V_{tot}[b]	D[c]
ZAP-LDH	72.96	0.030	23.51
α-ZnAl$_2$O$_4$	206.13	0.337	7.02
β-ZnAl$_2$O$_4$	155.79	0.392	8.42

[a]BET surface area (m^2/g)
[b]Total pore volume (cm^3/g)
[c]Average pore diameter (nm)

These burned materials construct increasing in sizes and pore volumes in a mesoporous scale at a temperature above 550 °C. Furthermore, nitrogen adsorption–desorption isotherms confirm slit-like structures on the pores as favorable porous materials.

3.4 Scanning electron microscopy morphology analysis

Scanning electron microscopy (SEM) surfaces material morphologies of ZAP-LDH, α-ZnAl$_2$O$_4$, and β-ZnAl$_2$O$_4$ are shown in Fig. 5. A uniformly ZAP-LDH sample derives numerous and regular pores as flake-like structures (Fig. 5a). The calcined samples obtain different morphologies depending on temperatures. For example, eliminated organic compounds as carbon cores and volatile substances assert lamellar structures breakdown into small pieces with pores at 700 °C and 800 °C (Fig. 5b, c). However, an anion-exchange route followed by heating treatment turns ZAP-LDH material to carbon dioxide, mixed metal oxides as spinel-type, and water. In Fig. 5d, the chemical composition from the EDX spectra reveals that the ratio of stoichiometric atom concentration is Zn:Al:O $\approx$ 14.6%:30.54%:54.86% $\approx$ 1:2:4, indicating that the as-obtained product is ZnAl$_2$O$_4$.

3.5 Comparison method

Table 3 offers different methods as a comparison from some physical properties. In this work, the results of ZnAl$_2$O$_4$ obtain a high surface area, a superior route, and comparable material. Otherwise, the other ways need a high energy source and outcome low surface area, but this anion-exchange technique followed by calcination receives an efficient energy source for synthesis. Also, the anion-substitute process acquires high pore volume, small crystallite size, and high surface area. This process produces suitable materials for catalytic purposes.

The photocatalytic reaction process of the α-ZnAl$_2$O$_4$ catalyst was studied by reducing pNP to pAP and was recorded using a UV–Vis spectrometer. Scheme 2 illustrates

Fig. 5 Scanning electron microscopy images of the ZAP-LDH (**a**), α-ZnAl$_2$O$_4$ (**b**), β-ZnAl$_2$O$_4$ (**c**), and EDX spectra of the α-ZnAl$_2$O$_4$ product (**d**)
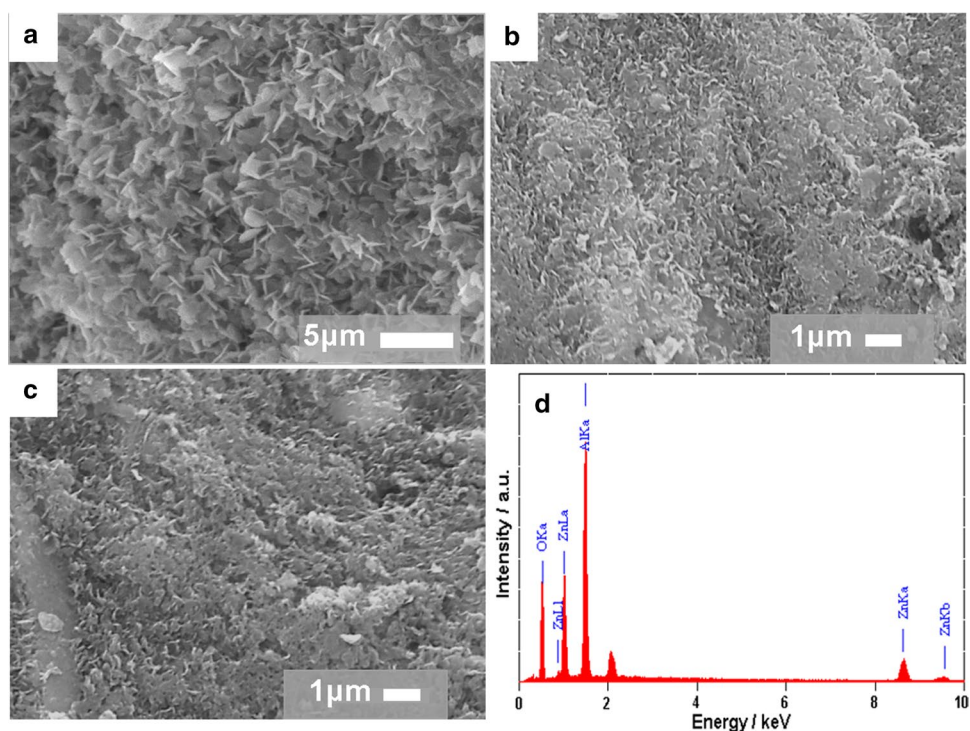

Table 3 Comparison of some physical properties of ZnAl$_2$O$_4$ spinel prepared by different methods

| Synthesis method	Temperature[a]	S_{BET}[b]	V_{tot}[c]	Size[d]	References
Anion exchange-heating treatment	700	206.13	0.337	9.3	Our work
Metal-chitosan complexation	700	162.25	0.333	5.0	[49]
	750	158.10	0.302	7.3	[50]
Green biosynthesis	900	14.40	0.054	64.0	[51]
Solvothermal	700	151.00	0.260	3–16	[52]
Co-precipitation	750	93.00	0.200	25.0	[53]
Sol–gel technique	800	124.80	0.299	10–30	[54]

[a]Temperature (°C)
[b]BET surface area (m^2/g)
[c]Total pore volume (cm^3/g)
[d]Mean crystallite size (nm)

a reduction from pNP to pAP with excess sodium borohydride in aqueous solution to evaluate catalytic properties at several reaction times. The complete hydrogenation was identified by changing color from bright yellow (pNP) to colorless (pAP). Besides, the conversion of pNP to pAP was changed the nitro group by the amine group. The addition of NaBH$_4$ as a reducing agent presents an effective technique to reduce pNP with metal catalysts under alkaline conditions. The reduction mechanism of pNP in aqueous solution over α-ZnAl$_2$O$_4$ can be expressed as

$$NaBH_4 \ (aq) \longrightarrow Na^+ + BH_4^- \tag{2}$$
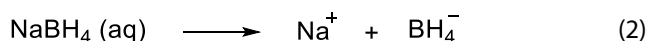
Scheme 2 The schematic reduction reaction of pNP to pAP in presence of the α-ZnAl$_2$O$_4$ catalyst and excess aqueous sodium borohydride
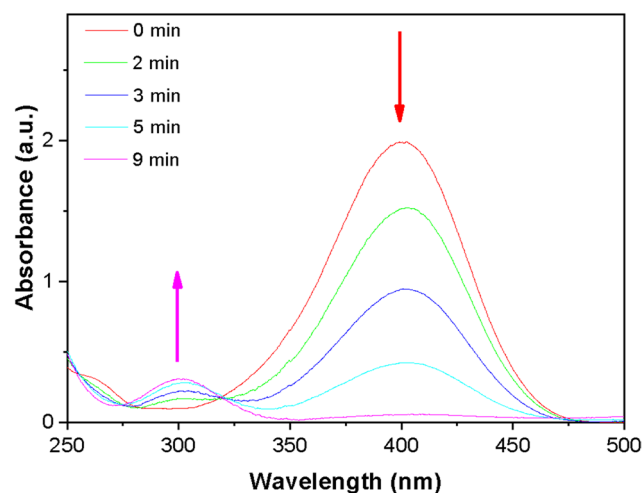

(3)

(4)

(5)

(6)
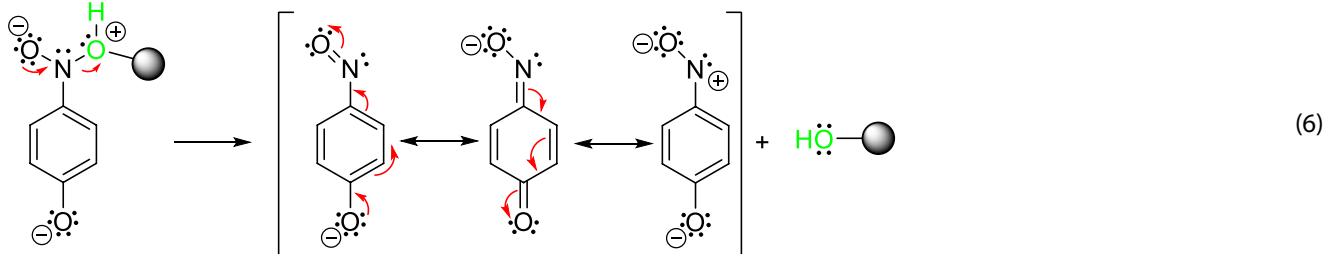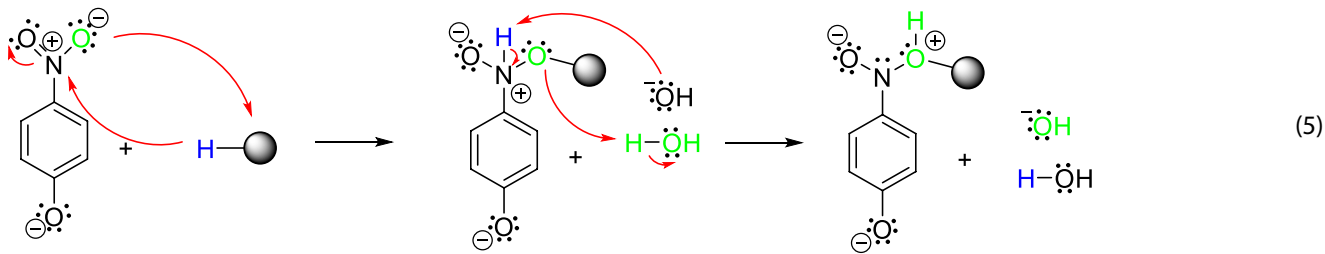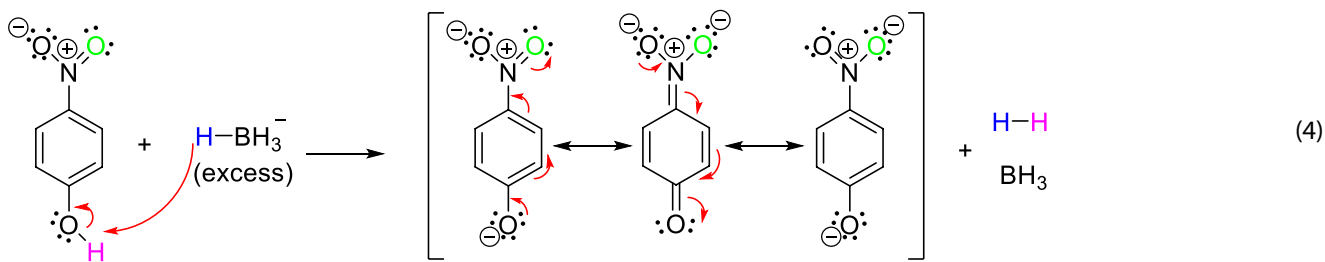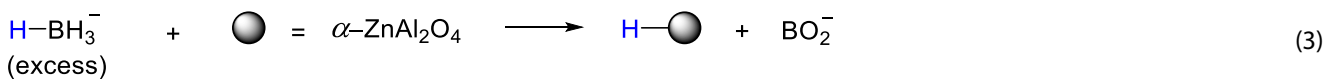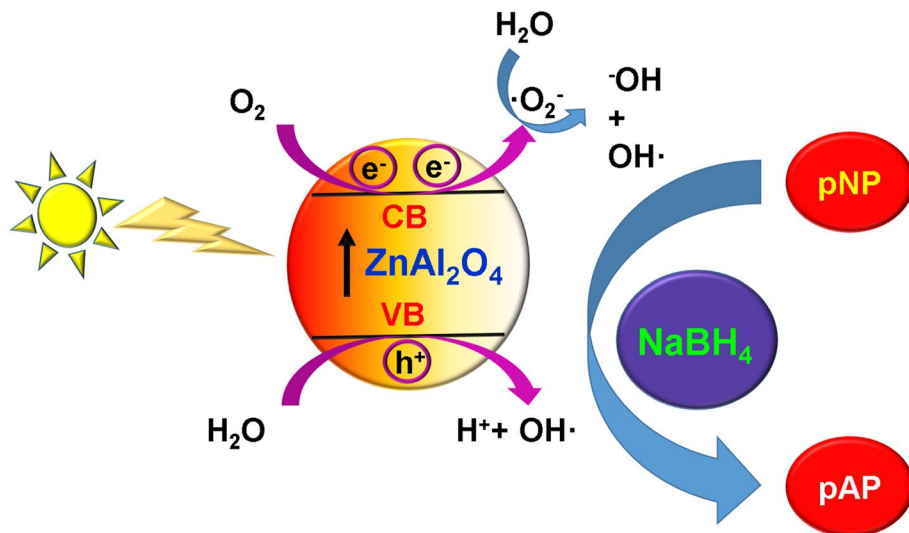
Fig. 6 UV–Vis absorption spectra of pNP by NaBH$_4$ in the presence of the catalyst

surface and the final reaction produces other metaborate anions.

The catalytic reaction can be completed within 9 min when the α-ZnAl$_2$O$_4$ spinel as a catalyst has been added into the cuvette. The best catalytic capacity possesses high surface area and rate of surface absorption. Adsorption of the reactant on the catalyst takes place electron transfers from BH$_4^-$ to pNP. First, the pNP reacts with NaBH$_4$ to produce p-nitrophenolate ($\lambda_{max} = 400$ nm). Second, the p-nitrophenolate and excess borohydride obtain an independent reaction in the presence of α-ZnAl$_2$O$_4$ spinel. In addition, a peak intensity of p-nitrophenolate presents a decrease rapidly corresponding in the color from bright yellow to colorless, but a new intensity of p-aminophenol peak ($\lambda_{max} = 300$ nm) appears an increase gradually (Fig. 6).

(7)

(8)
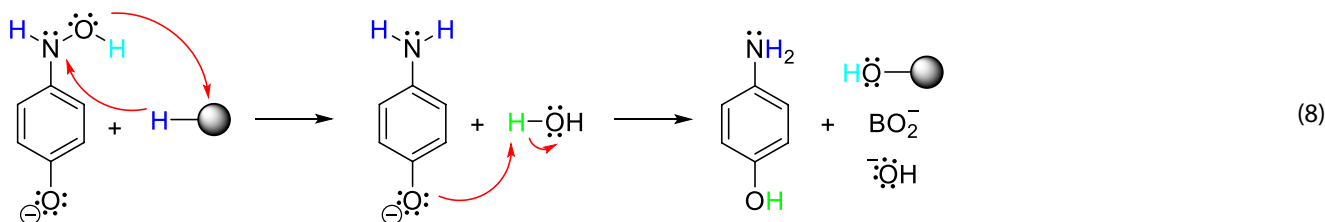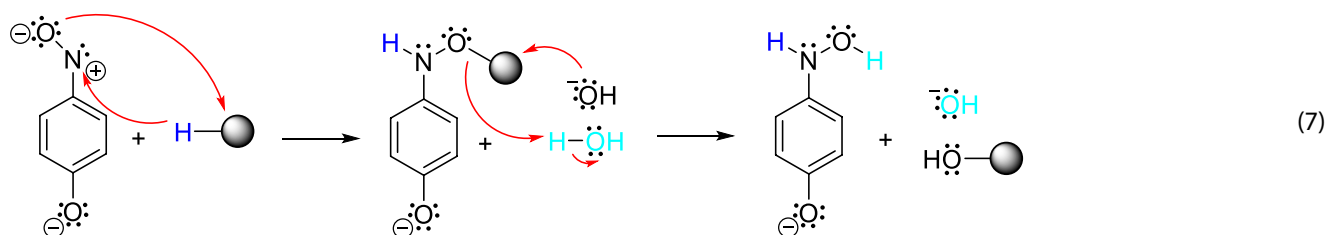
Sodium borohydride (NaBH$_4$) in aqueous solution forms sodium cation (Na$^+$) and borohydride anion (BH$_4^-$). The BH$_4^-$ fabricates activated hydrogen (H$^-$) and metaborate (BO$_2^-$) after reacting with H$_2$O. Furthermore, the combination of activated hydrogen and α-ZnAl$_2$O$_4$ obtains new species as H-α-ZnAl$_2$O$_4$ on the surface of the catalyst. Hydrogen atom on alcohol functional group of pNP is interacted with the hydrogen of borohydride anion to fabricate p-nitrophenolate and H$_2$. However, the oxygen on the nitro group of p-nitrophenolate is substituted by activated hydrogen during the reaction to form the amine group of pAP via electron transfer on the catalyst surface. Therefore, the resulted pAP is desorbed from the catalyst

4 Conclusions

This study has been investigated by visible-light-active α-ZnAl$_2$O$_4$ calcined from anion-exchange LDH. The effect of anion exchange LDH followed by the heat process presents the best material of the mesoporous scale. The α-ZnAl$_2$O$_4$ spinel provides more active sites to adsorb reactant molecules as photocatalysts. Complete conversion of p-nitrophenol to p-aminophenol was reached after 9 min under visible irradiation. Furthermore, total pore volume and BET surface area were obtained 0.337 cm^3/g and 206.13 m^2/g, respectively. In conclusion, the active α-ZnAl$_2$O$_4$ spinel is claimed as a high surface area

material, a comparable product, a superior method, and an effective reducing agent.

Code availability 92E99.

Compliance with ethical standards

Conflict of interest On behalf of the author, the corresponding author states that there is no conflict of interest.

Ethical approval This article does not contain any studies with human participants or animals performed by any of the authors.

References

1. Ren Y, Zhou J, Pan Z, Lai B, Yuan D (2019) Rapid removal of ultra-high concentration p-nitrophenol in aqueous solution by microwave enhanced Fe/Cu bimetallic particle (MW-Fe/Cu) system. Environ Technol 40(2):239–249

2. El-Shafey SE, Fathy NA, Khalil LB (2017) Abatement of p-nitrophenol from aqueous solutions using oxidized carbon fiber. Egypt J Chem 60(6):995–1006

3. You N, Li JY, Fan HT, Shen H (2019) In-situ sampling of nitrophenols in industrial wastewaters using diffusive gradients in thin films based on lignocellulose-derived activated carbons. J Adv Res 15:77–86

4. Cheng M, Jiang J, Wang J, Fan J (2019) Highly salt resistant polymer supported ionic liquid adsorbent for ultrahigh capacity removal of *p*-nitrophenol from water. ACS Sustain Chem Eng 7(9):8195–8205

5. Ren W, Gao J, Lei C, Xie Y, Cai Y, Ni Q, Yao J (2018) Recyclable metal-organic framework/cellulose aerogels for activating peroxymonosulfate to degrade organic pollutants. Chem Eng J 349:766–774

6. Elisashvili V, Kachlishvili E, Asatiani MD (2018) Efficient production of lignin-modifying enzymes and phenolics removal in submerged fermentation of olive mill by-products by white-rot basidiomycetes. Int Biodeter Biodegr 134:39–47

7. Yelatontsev D, Suprunchuk V, Voloshin M (2017) Sedimentation of pollutant-containing aggregates during purification of wastewater from coking plants. East-Eur J Enterp Technol 6(10):38–44

8. Sahu K, Singh J, Mohapatra S (2019) Catalytic reduction of 4-nitrophenol and photocatalytic degradation of organic pollutants in water by copper oxide nanosheets. Opt Mater 93:58–69

9. Mohan BS, Ravi K, Anjaneyulu RB, Sree GS, Basavaiah K (2019) Fe_2O_3/RGO nanocomposite photocatalyst: effective degradation of 4-nitrophenol. Phys B 553:190–194

10. Sinha T, Ahmaruzzaman Md, Adhikari PP, Bora R (2017) Green and environmentally sustainable fabrication of Ag-SnO_2 nanocomposite and its multifunctional efficacy as photocatalyst and antibacterial and antioxidant agent. ACS Sustain Chem Eng 5(6):4645–4655

11. Mahy JG, Paez CA, Carcel C, Bied C, Tatton AS et al (2019) Porphyrin-based hybrid silica-titania as a visible-light photocatalyst. J Photochem Photobiol 373:66–76

12. Tong H, Zhan X, Tian X, Li J, Qian D et al (2018) Understanding the energy level matching relationships between semiconductor photocatalysts and organic pollutants for effective photocatalytic degradations. J Colloid Interface Sci 526:384–391

13. Nguyen VQ, Baynosa ML, Nguyen VH, Tuma D, Lee YR et al (2019) Solvent-driven morphology-controlled synthesis of highly efficient long-life ZnO/graphene nanocomposite photocatalysts for the practical degradation of organic wastewater under solar light. Appl Surf Sci 486:37–51

14. Benhebal H, Wolfs C, Kadi S, Tilkin RG, Allouche B et al (2019) Visible light sensitive SnO_2/$ZnCo_2O_4$ material for the photocatalytic removal of organic pollutants in water. Inorganics 7(6):77–98

15. Asl EA, Haghighi M, Talati A (2019) Sono-solvothermal fabrication of flowerlike $Bi_7O_9I_3$-$MgAl_2O_4$ p-n nano-heterostructure photocatalyst with enhanced solar-light-driven degradation of methylene blue. Sol Energy 184:426–439

16. Kumar A, Rout L, Achary LSK, Mohanty SK, Dash P (2017) A combustion synthesis route for magnetically separable graphene oxide-$CuFe_2O_4$-ZnO nanocomposites with enhanced solar light-mediated photocatalytic activity. New J Chem 4:10568–10583

17. Behera A, Kandi D, Majhi SM, Martha S, Parida K (2018) Facile synthesis of $ZnFe_2O_4$ photocatalysts for decolourization of organic dyes under solar irradiation. Beilstein J Nanotechnol 9:436–446

18. Xu Y, Lin Z, Zheng Y, Dacquin JP, Royer S et al (2019) Mechanism and kinetics of catalytic ozonation for elimination of organic compounds with spinel-type $CuAl_2O_4$ and its precursor. Sci Total Environ 651(2):2585–2596

19. De K, Mukhopadhyay C (2018) $ZnFe_2O_4$ nanoparticles: an efficient and recyclable catalyst for the synthesis of isatinylidenethiazol-4-one derivatives. ChemistrySelect 3(24):6873–6879

20. Appiah-Ntiamoah R, Baye AF, Gadisa BT, Abebe MW, Kim H (2019) In-situ prepared ZnO-$ZnFe_2O_4$ with 1-D nanofiber network structure: an effective adsorbent for toxic dye effluent treatment. J Hazard Mater 373:459–467

21. Gopinath A, Kadirvelu K (2019) Preparation and characterization of mixed metal oxide $ZnCo_2O_4$ spinel coated ACF for environmental remediation. Mater Res Express 6(4):6518–6538

22. Euch SEL, Bricault D, Cachet H, Sutter EMM, Tran MTT et al (2019) Temperature dependence of the electrochemical behavior of the 690 Ni-base alloy between 25 and 325 °C. Electrochim Acta 317:509–520

23. Bosi F, Biagioni C, Pasero M (2019) Nomenclature and classification of the spinel supergroup. Eur J Mineral 31(1):183–192

24. Regulska E, Breczko J, Basa A (2019) Pristine and graphene-quantum-dots-decorated spinel nickel aluminate for water remediation from dyes and toxic pollutants. Water 11(5):953–968

25. Liu Q, Xiong Z, Syed-Hassan SSA, Deng Z, Zhao X et al (2019) Effect of the pre-reforming by Fe/bio-char catalyst on a two-stage catalytic steam reforming of bio-oil. Fuel 239:282–289

26. Arandia A, Coronado I, Remiro A, Gayubo AG, Reinikainen M (2019) Aqueous-phase reforming of bio-oil aqueous fraction over nickel-based catalysts. Int J Hydrogen Energy 44(26):13157–13168

27. Zhou R, Zhao J, Shen N, Ma T, Su Y et al (2018) Efficient degradation of 2,4-dichlorophenol in aqueous solution by peroxymonosulfate activated with magnetic spinel $FeCo_2O_4$ nanoparticles. Chemosphere 197:670–679

28. Xu H, Wang D, Ma J, Zhang T, Lu X et al (2018) A superior active and stable spinel sulfide for catalytic peroxymonosulfate oxidation of bisphenol S. Appl Catal B 238:557–567

29. Pi L, Yang N, Han W, Xiao W, Xiong Y et al (2018) Heterogeneous activation of peroxymonocarbonate by Co-Mn oxides for the efficient degradation of chlorophenols in the presence of a naturally occurring level of bicarbonate. Chem Eng J 334:1297–1308

30. Tangcharoen T, Thienprasert J, Kongmark C (2018) Optical properties and versatile photocatalytic degradation ability of

MAl_2O_4 (M = Ni, Cu, Zn) aluminate spinel nanoparticles. J Mater Sci 29(11):8995–9006

31. Hu L, Zhang G, Liu M, Wang Q, Wang P (2018) Optimization of the catalytic activity of a $ZnCo_2O_4$ catalyst in peroxymonosulfate activation for bisphenol A removal using response surface methodology. Chemosphere 212:152–161

32. Yu Z, Moussa H, Chouchene B, Liu M (2019) One-step synthesis and deposition of $ZnFe_2O_4$ related composite films via SPSS route for photodegradation application. Nanotechnology 30(4):5707–5743

33. Kadhim SH (2018) Synthesis, characterization and catalytic activity of $NiO-Mn_2O_3/ZrO_2$ spinel Co-catalysts. Asian J Chem 30(7):1650–1654

34. Shi Y, Tang X, Yi H, Gao F, Zhao S et al (2019) Controlled synthesis of spinel-type mesoporous Mn-Co rods for SCR of NO_x with NH_3 at low temperature. Ind Eng Chem Res 58(9):3606–3617

35. Xu X, Xiao L, Jia Y, Hong Y, Ma J et al (2018) Strong visible light photocatalytic activity of magnetically recyclable sol-gel-synthesized $ZnFe_2O_4$ for rhodamine B degradation. J Electron Mater 47:536–541

36. Vinosha PA, Xavier B, Anceila D, Das SJ (2018) Nanocrystalline ferrite (MFe_2O_4, M=Ni, Cu, Mn, and Sr) photocatalysts synthesized by homogeneous Co-precipitation technique. Optik 157:441–448

37. Yakob M, Umar H, Wahyuningsih P, Putra RA (2019) Characterization of microstructural and optical $CoFe_2O_4/SiO_2$ ferrite nanocomposite for photodegradation of methylene blue. AIMS Mater Sci 6(1):45–51

38. Douafer S, Lahmar H, Benamira M, Rekhila G, Trari M (2018) Physical and photoelectrochemical properties of the spinel LiMn2O4 and its application in photocatalysis. J Phys Chem Solids 118:62–67

39. Chen M, Wu P, Wei Q, Zhu Y, Yang S et al (2018) The role of oxygen vacancy over ZnCr-layered double oxide in enhancing solar light-driven photocatalytic degradation of bisphenol A. Environ Chem 15(4):226–235

40. Huang MX, Wu X, Yi XD, Han GB, Xia WS et al (2017) Highly dispersed CoO_x in layered double oxides for oxidative dehydrogenation of propane: guest-host interactions. RSC Adv 7:14846–14856

41. Ortega KF, Rein D, Lüttmann C, Heese J, Özcan F et al (2016) Ammonia decomposition and synthesis over multinary magnesioferrites: promotional effect of Ga on Fe catalysts for the decomposition reaction. ChemCatChem 9(4):659–671

42. Li D, Xu S, Cai Y, Chen C, Zhan Y et al (2017) Characterization and catalytic performance of $Cu/ZnO/Al_2O_3$ water-gas shift catalysts derived from Cu-Zn-Al layered double hydroxides. Ind Eng Chem Res 56(12):3175–3183

43. Li D, Fan Y, Ding Y, Wei X, Xiao Y (2017) Preparation of cobalt-copper-aluminum spinel mixed oxides from layered double hydroxides for total oxidation of benzene. Catal Commun 88:60–63

44. Răciulete M, Layrac G, Papa F, Negrilă C, Tichit D et al (2018) Influence of Mn content on the catalytic properties of Cu-(Mn)-Zn-Mg-Al mixed oxides derived from LDH precursors in the total oxidation of methane. Catal Today 306:276–286

45. Huo L, Liu B, Li H, Cao B, Hu XC et al (2019) Component synergy and armor protection induced superior catalytic activity and stability of ultrathin Co-Fe spinel nanosheets confined in mesoporous silica shells for ammonia decomposition reaction. Appl Catal B 253:121–130

46. Meng W, Li F, Evans DG, Duan X (2004) Photocatalytic activity of highly porous zinc ferrite prepared from a zinc-iron(III)-sulfate layered double hydroxide precursor. J Porous Mat 11(2):97–105

47. Liu Y, Wang H, Xiong C, Chai Y, Yuan R (2017) An ultrasensitive electrochemiluminescence immunosensor for NT-proBNP based on self-catalyzed luminescence emitter coupled with PdCu@carbon nanohorn hybrid. Biosens Bioelectron 15(87):779–785

48. Rana U, Chakrabarti K, Malik S (2011) *Insitu* preparation of fluorescent polyanilinenanotubes doped with perylenetetracarboxylic acids. J Mater Chem 21:11098–11100

49. Stringhini FM, Foletto EL, Sallet D, Bertuol DA, Filho OC et al (2014) Synthesis of porous zinc aluminate spinel ($ZnAl_2O_4$) by metal-chitosan complexation method. J Alloy Compd 588:305–309

50. Anchieta CG, Sallet D, Foletto EL, da Silva SS, Filho OC et al (2014) Synthesis of ternary zinc spinel oxides and their application in the photodegradation of organic pollutant. Ceram Int 40(3):4173–4178

51. Gholami T, Niasari MS, Sabet M (2018) Novel green synthesis of $ZnAl_2O_4$ and $ZnAl_2O_4$/graphene nanocomposite and comparison of electrochemical hydrogen storage and Coulombic efficiency. J Clean Prod 178:14–21

52. Staszak W, Zawadzki M, Okal J (2010) Solvothermal synthesis and characterization of nanosized zinc aluminate spinel used in *iso*-butane combustion. J Alloy Compd 492(1–2):500–507

53. Battiston S, Rigo C, Severo EC, Mazutti MA, Kuhn RC et al (2014) Synthesis of zinc aluminate ($ZnAl_2O_4$) spinel and its application as photocatalyst. Mat Res 17(3):734–738

54. Saikia P, Goswamee R (2018) The effect of strength of bases and temperature on the synthesis of Zn-Al layered double hydroxides by a non-aqueous 'soft chemical' sol-gel method and formation of high surface area mesoporous $ZnAl_2O_4$ spinel. ChemistrySelect 3(26):7619–7626